Automatica 155 (2023) 111119

Contents lists available at ScienceDirect

Automatica

journal homepage: www.elsevier.com/locate/automatica

Brief paper

Flight data validation of an icing accretion estimation scheme using super-twisting observers☆

Lejun Chen [a,*], James F. Whidborne [b]

[a] Department of Electronics and Electrical Engineering, University College London, UK
[b] School of Aerospace, Transport and Manufacturing, Cranfield University, UK

ARTICLE INFO

Article history:
Received 28 June 2022
Received in revised form 21 December 2022
Accepted 3 April 2023
Available online 15 June 2023

Keywords:
Sliding mode observer
Fault estimation
Icing accretion

ABSTRACT

This paper develops a generalised multivariable super-twisting observer for a class of nonlinear systems in which the unmeasured variables linked to the known state dependent matrix function appear multiplicatively. A sufficient condition is given to guarantee that the reconstruction errors associated with the unmeasurable variables converge to zero in finite time. This approach is then used to address the aircraft icing accretion estimation problem despite unreliable sensor measurement. The efficacy of the approach has been evaluated via real flight data recorded under natural icing conditions. Results show that the observer has the capability to estimate the change of the drag coefficient induced by icing accretion and to reconstruct the unreliable pitch rate sensor measurement simultaneously.

1. Introduction

Aircraft icing is one of the most hazardous flight conditions for both manned aircraft and Unmanned Aerial Vehicles (UAVs). Despite icing research having been systematically conducted for over 70 years, it remains a key issue. The National Transportation Safety Board found that between 2008 and 2016 there were 46 aircraft accidents where in-flight icing was a cause or factor (FAA, 2020). Other recent losses where icing was a contributory factor include Air Algérie Flight 5017 (N'Faly, 2016) in 2014, West Wind Aviation Flight 282 (Transportation Safety Board of Canada, 2021) and the Myanmar Air Force Shaanxi Y-8 accident (BBC, 2017), both in 2017. Reliable identification of icing conditions and their severity can improve pilot situational awareness so that the de-icing and anti-icing systems and procedures can be invoked effectively and so improve the aircraft safety. In addition, identification or estimation of the icing accretion is extremely important for UAVs where the lack of an on-board pilot makes situational awareness more critical; and for autonomous operation of UAVs, an icing identification capability is even more important (Armanini, Polak, Gautrey, Lucas, & Whidborne, 2016; Sorensen, Blanke, & Johansen, 2015).

Indeed, ice accretion represents a serious hazard to aircraft safety. Ice accumulates on every exposed frontal surface of an aircraft. This includes wing and empennage leading edges, propellers and spinners, engine intakes, landing gear, windshield, antennas and other miscellaneous areas. As a result of ice accretion, significant aerodynamic penalties are observed. Drag is increased and changes in pressure distribution and early boundary layer separation leads to a decrease in lift and stall angle. In order to maintain constant speed and altitude, the pilot will normally compensate these aerodynamic penalties by adding more power and lifting the nose up to increase Angle of Attack (AoA). On the other hand this action will only expose the underside of the wing and fuselage to additional ice accumulation. With the successive increase of ice, there is a risk that the aircraft will not have enough performance to climb or accelerate or even worse, it can come to the point where the aircraft will start to roll and pitch un-controllably and its recovery will be impossible.

Aircraft certified for flight in icing conditions are usually equipped with de-icing systems which remove accreted ice, and anti-icing systems which prevent icing accretion. For manned aircraft the responsibility for the icing management lies with the pilot who watches for ice formation on the windscreen, wings and other visible aircraft components. In addition, many aircraft are equipped with icing sensors. However, for unmanned aircraft, maintaining the same level of situational awareness for the remote pilot is difficult. Although aircraft may be equipped with icing sensors and cameras, these add weight and other overheads. Furthermore, both the amount and location of ice accretion depends on the aircraft shape as well as the weather and flight conditions. Thus the problem of icing diagnosis is very important and difficult.

☆ The material in this paper was not presented at any conference. This paper was recommended for publication in revised form by Associate Editor Peng Shi under the direction of Editor Thomas Parisini.

* Corresponding author.
E-mail addresses: Lejun.Chen@ucl.ac.uk (L. Chen), j.f.whidborne@cranfield.ac.uk (J.F. Whidborne).

https://doi.org/10.1016/j.automatica.2023.111119

One of the biggest challenges for icing research is to find out a solution to characterise, diagnose and estimate the severity of icing accretion (Lampton & Valasek, 2007). Over the last two decades, many icing diagnosis methods have been proposed in the literature. For example, the work in Dong (2018) and Schuchard, Melody, Başar, Perkins, and Voulgaris (2000) applied neural networks to monitor icing and its effects upon performance, stability and control. The innovation sequence based methods, including the Kalman filtering method and its variants, were also developed for the purpose of icing detection (Caliskan, Aykan, & Hajiyev, 2008; Melody, Başar, Perkins, & Voulgaris, 2000). In Melody et al. (2000) and Melody, Hillbrand, Başar, and Perkins (2001), the coordination between aircraft stability and control derivatives and the icing severity factor was established via a linear interpolation between the iced and clean aircraft models. Furthermore, the $\mathcal{H}_\infty$ based algorithm was exploited to detect icing on the NASA Twin Otter inflight icing research aircraft model. In recent years, model-based observer design methods have been successfully applied to solve icing diagnosis problems. One of the earliest works in Miller and Ribbens (1999) modelled the onset of aircraft tail icing as a partial actuator failure and a gain-scheduled Luenberger observer was designed to detect the icing severity. Some recent works extended the linear time invariant unknown input observer (UIO) method to one in the linear parameter varying (LPV) framework and applied it to UAV icing detection problems (Cristofaro & Johansen, 2015; Rotondo, Cristofaro, Johansen, Nejjari, & Puig, 2018, 2019). In Cristofaro, Johansen, and Aguiar (2015), a multiple model adaptive estimation framework (Sastry & Bodson, 1989) was developed to estimate icing severity for UAVs.

The topic of fault tolerant control (FTC) has been widely developed over the last decade (Alwi, Edwards, & Tan, 2011; Blanke, Kinnaert, Lunze, & Staroswiecki, 2016; Chen & Patton, 1999; Ding, 2013; Edwards, Lombaerts, & Smaili, 2010; Zhang & Jiang, 2008) and many different paradigms have subsequently been applied to problems in the aerospace sector (Goupil, Dayre, & Brot, 2014; Marcos, Waitman, & Sato, 2021). Sliding mode observers (SMOs) (Chen, Edwards, & Alwi, 2019; Edwards & Spurgeon, 1998; Efimov, Edwards, & Zolghadri, 2016; Elleuch, Khedher, & Othman, 2018; de Loza, Bejarano, & Fridman, 2013; Utkin, 1992; Yan & Edwards, 2008) have been widely applied to solve fault diagnosis problems of flight control and one has been successfully implemented and validated via actual flight tests (Chen, Alwi, Edwards, & Sato, 2020, 2022). In Edwards and Spurgeon (1998), the first order SMO was first employed for the purpose of fault reconstruction, a major drawback this approach is the chattering phenomenon, so additional low pass filters and continuous approximation functions are often applied to the classical first-order SMO to reduce chattering appearing in the error injection. The variable gain super-twisting algorithms (STAs) have been well developed to compensate for state dependent perturbations (Castillo, Fridman, & Moreno, 2018; Gonzalez, Moreno, & Fridman, 2012). Ref. Oliveira, Estrada, and Fridman (2017) generalised the work in Gonzalez et al. (2012) and developed output feedback STAs for scalar systems where the upper bound of the unmeasured state vector and the perturbations were obtained by state norm observers. This approach was then extended by Oliveira, Rodrigues, Estrada, and Fridman (2018) and Rodrigues and Oliveira (2018) to consider arbitrary relative degree systems and to develop an adaptive differentiator. In Rodrigues and Oliveira (2022), this approach was improved to take into account a class of multivariable systems. Some other representative STAs have also been developed for multivariable systems involving state-dependent perturbations (e.g. in Nagesh and Edwards (2014) and Vidal, Nunes, and Hsu (2017)). Most recently, Moreno, Rios, Ovalle, and Fridman (2022) considers the situation in which both the uncertain control distribution function and the perturbation are both state dependent. Although the state dependent perturbations were considered in Gonzalez et al. (2012), Oliveira et al. (2017, 2018), Rodrigues and Oliveira (2018, 2022) and Vidal et al. (2017), the control inputs or the gradient of non-vanishing perturbation terms in the dynamic extension were assumed to be bounded a priori. In addition, the structural constraints of the triple (A, B, C) need to be satisfied.

One of the motivations of applying super-twisting sliding mode observers (Guzman & Moreno, 2015; Levant, 1998; Moreno & Alvarez, 2014) to the icing estimation problem is that the discontinuous injection terms allow unknown inputs to be exactly reconstructed in finite time despite the uncertain rates of the unknown inputs. This property, which is not possessed by continuous observers (e.g. linear Luenberger observers Miller & Ribbens, 1999 or high gain observers), is well posed for estimating icing accretion since knowledge of the accretion rate in natural flight conditions is not available in real time. Compared with quasi-LPV UIOs proposed in Cristofaro and Johansen (2015) and Rotondo et al. (2018, 2019), the icing severity is exactly estimated instead of being diagnosed using residual generators. Also the initial conditions of the plant/observer is not required to be known and the hypothesis of accurate measurements of the scheduling parameters and structural algebraic conditions of systems are not imposed. Compared with Kalman filtering and its variants (Caliskan et al., 2008; Melody et al., 2000), the probability distributions with respect to model/measurement uncertainties are not defined a priori. Compared with adaptive multiple model observers (Cristofaro et al., 2015), the icing severity factor is not assumed to be slowly varying. Furthermore, by using super twisting observers, known functions are not necessary to satisfy the globally or locally Lipschitz conditions. In the literature, super twisting observers were usually developed for scalar systems and it is not straightforward to analyse the finite time convergence for multivariable systems, especially when the unmeasured variables linked to the known state dependent matrix function appears multiplicative.

The main theoretical contribution of this paper is to develop a generalised multivariable super-twisting observer to estimate the unmeasurable variables, pre-multiplied by a state dependent matrix, exactly and in finite time, whilst improving the design conservatism by choosing the state dependent modulation gains. By introducing an extra design freedom, the order of dynamic extension of the STAs associated with the unmeasured state augmentation is equivalent to one of the output vector. This forms the basis for the construction of generalised multivariable STAs. Compared with the STAs proposed in Gonzalez et al. (2012), Oliveira et al. (2017, 2018), Rodrigues and Oliveira (2018, 2022) and Vidal et al. (2017), the hypothesis of a bounded gradient of non-vanishing perturbation (i.e. the term involving the estimation error associated with the unmeasured state augmentation) is no longer required. This effectively solves the algebraic loop problem (Castillo et al., 2018) of conventional STAs, i.e. the gradient of non-varnishing perturbation depends on the dynamics of the estimation error (or the observer dynamics) itself, which increases the perturbation exponentially. This improvement also allows the initial value of the state estimation error to be arbitrarily large. Furthermore, the structural constraints of the triple (A, B, C) is released and therefore this proposed algorithm is well posed for more general nonlinear systems. In this paper, the selection of a quadratic Lyapunov function with a simple time-invariant, non-smooth Lyapunov function is discussed. Finally, the design scheme is used to estimate the change of the drag coefficient induced by natural icing accretion (without knowledge of the accretion rate) and to reconstruct the unreliable pitch rate measurement. To further

demonstrate its practicality, this scheme is validated using real flight data recorded from the Cranfield University Jetstream J31 aircraft under natural icing conditions (Armanini et al., 2016). To the authors' best knowledge, this paper shows the first time the generalised super-twisting observer based icing estimation scheme is validated using real flight data.

The notation in this paper is standard. For example, $A > 0$ denotes a positive definite matrix, and the symbol $\|\cdot\|$ denotes the Euclidean norm or its induced norm.

2. Multivariable super-twisting observer design

In this section, a super-twisting observer with state dependent gains theory underpinning for a class of nonlinear systems is developed.

Consider a class of nonlinear systems

$$\begin{aligned}\dot{x}_1(t) &= f_1(x_1,u) + F(y,u,t)x_2(t)\\ \dot{x}_2(t) &= f_2(x_1,u) + \xi(t)\\ y(t) &= x_1(t)\end{aligned} \tag{1}$$

where $x_1 \in \mathbb{R}^n$, $x_2 \in \mathbb{R}^l$ are system states, $u \in \mathbb{R}^m$ denote system inputs, $y(t) \in \mathbb{R}^n$ are system outputs. $f_1(x_1,u) : \mathbb{R}^n \times \mathbb{R}^m \to \mathbb{R}^n$, $f_2(x_1,u) : \mathbb{R}^n \times \mathbb{R}^m \to \mathbb{R}^l$ are vector functions. The known matrix function $F(y,u,t) \in \mathbb{R}^{n\times l}$, and the unknown but bounded signal $\xi(t) \in \mathbb{R}^l$ denotes an external disturbance. It is assumed that system (1) has solutions in the sense of Filippov (1988).

Remark 2.1. Since the state vector $x_2(t)$ is multiplied by the time-varying matrix $F(y,u,t)$, $x_2(t)$ cannot be reconstructed exactly and in finite time by using conventional continuous observers. Also this work does not divide the joint variable $F(y,u,t)x_2(t)$ by $F(y,u,t)$ such that the pathological condition in which $F(y,u,t)$ is too small can be avoided.

For the developments which follow the system in (1) is rewritten as

$$\begin{aligned}\dot{x}_1(t) &= f_1(x_1,u) + E(y,u,t)\tilde{x}_2(t)\\ \dot{\tilde{x}}_2(t) &= \tilde{f}_2(x_1,u) + \tilde{\xi}(t)\\ y(t) &= x_1(t)\end{aligned} \tag{2}$$

where $E(y,u,t) \in \mathbb{R}^{n\times n}$ is defined as $E(y,u,t) = [F(y,u,t)\ \ H]$, $\tilde{x}_2(t) = [x_2(t)^T\ 0]^T \in \mathbb{R}^n$, $\tilde{f}_2(x_1,u) = [f_2^T(x_1,\rho,u)\ 0]^T$ and $\tilde{\xi}(t) = [\xi(t)^T\ 0]^T$. Clearly this can be done without loss of generality (w.l.o.g). The matrix $H \in \mathbb{R}^{n\times(n-l)}$ represents the design freedom and it has no physical meaning. However since $E(y,u,t)$ will become one of the observer gains (associated with the nonlinear injection signal), H may be viewed as part of the available observer design freedom.

The following assumptions are used throughout the paper.

Assumption 2.1. It is assumed that the design freedom H ensures $E(y,u,t)$ is positive definite (via a coordination transformation) and that the system in (2) is uniformly observable (Gauthier, Hammouri, & Othman, 1992).

Assumption 2.2. The matrix $E(y,u,t)$ in (2) satisfies

$$0 < \delta_1 \le \|E(y,u,t)\| \le \delta_2 \tag{3}$$

where δ_1 and δ_2 are known fixed scalars.

Remark 2.2. The design freedom H allows the upper/lower bound of $E(y,u,t)$ to be flexibly chosen such that the lower bound of the modulation gain can be tuned.

2.1. Observer formulation

The observer is chosen to have the structure

$$\begin{aligned}\dot{\hat{x}}_1(t) &= -k_1(y,t)E(y,u,t)\phi_1(e_1) + f_1(\hat{x}_1,u)\\ &\quad + E(y,u,t)(\hat{x}_2(t) + \Psi e_1(t))\\ \dot{\hat{x}}_2(t) &= -k_2(y,t)\phi_2(e_1) + \tilde{f}_2(\hat{x}_1,u)\end{aligned} \tag{4}$$

where $e_1 = \hat{x}_1 - x_1$ and $k_1(y,t), k_2(y,t) : \mathbb{R}^n \times \mathbb{R}^r \times \mathbb{R}^+ \to \mathbb{R}^+$ are state dependent modulation functions to be determined. The matrix $\Psi \in \mathbb{R}^{n\times n}$ is design freedom and its maximum eigenvalue λ_M satisfies

$$\lambda_M := \frac{\delta_1 - \beta}{2\delta_2} \tag{5}$$

where δ_1 and δ_2 are defined in (3) and the scalar β satisfies $\beta \in (0\quad \delta_1)$. In (4), the injection terms $\phi_1(e_1)$ and $\phi_2(e_1)$ are defined as

$$\begin{aligned}\phi_1(e_1) &:= \frac{e_1(t)}{\|e_1(t)\|^{\frac{1}{2}}} + k_3 e_1(t)\\ \phi_2(e_1) &:= \frac{1}{2}\frac{e_1(t)}{\|e_1(t)\|} + \frac{3}{2}\frac{e_1(t)}{\|e_1(t)\|^{\frac{1}{2}}} + k_3^2 e_1(t)\end{aligned} \tag{6}$$

where $k_3 > 0$. Notice that the structures of $\phi_1(e_1)$ and $\phi_2(e_1)$ are similar as those in Gonzalez et al. (2012). From (6), $\phi_1(e_1)$ and $\phi_2(e_1)$ satisfy

$$\phi_2(e_1) = (\nabla_{e_1}\phi_1)\phi_1(e_1) \tag{7}$$

which represents the property of generalised multivariable STAs.

Since the vector functions $f_1(\cdot)$ and $\tilde{f}_2(\cdot)$ in (4) only depend on $\hat{x}_1$, the following remark holds

Remark 2.3. The observer formulation in (4) does not require the initial conditions of the plant and the observer to be defined exactly.

Define $e_2 = \hat{x}_2 - \tilde{x}_2 + \Psi e_1(t)$, the error dynamics between (1) and (4) can be written as

$$\begin{aligned}\dot{e}_1(t) &= -k_1(y,t)E(y,u,t)\phi_1(e_1) + \tau_1(\cdot) + E(y,u,t)e_2(t)\\ \dot{e}_2(t) &= -k_2(y,t)\phi_2(e_1) + \tau_2(\cdot) + \Psi\dot{e}_1(t)\end{aligned} \tag{8}$$

and the perturbation vectors $\tau_1(\cdot)$ and $\tau_2(\cdot)$ are given by

$$\begin{aligned}\tau_1(e_1,y,u) &= f_1(x_1+e_1,u) - f_1(x_1,u)\\ \tau_2(e_1,y,u,\tilde{\xi}) &= \tilde{f}_2(x_1+e_1,u) - \tilde{f}_2(x_1,u) - \tilde{\xi}(t)\end{aligned} \tag{9}$$

Remark 2.4. The modulation function $k_2(y,t)$ in (8) must be selected to compensate the perturbation involving $\dot{e}_1(t)$ which depends on modulation gains $k_1(y,t)$ and $k_2(y,t)$. This raises the algebraic loop problem of conventional STAs (Castillo et al., 2018).

Remark 2.5. From Eq. (8), $\Psi\dot{e}_1(t)$ involves the term $-\Psi E(y,u,\tau)$ $k_2(y,\tau)\int_0^t \phi_2(e_1(\tau))d\tau$ which depends on the initial condition $e_1(0)$. Using conventional STAs, an upper bound of $\Psi\dot{e}_1(t)$ must be imposed and thus $e_1(0)$ cannot be arbitrarily large.

In the sequel, a multivariable variable gain STA will be proposed to ensure the occurrence of the second order sliding motion for (8).

Define the uncertain matrix functions $D_1(\cdot) \in \mathbb{R}^{n\times n}$ and $D_2(\cdot) \in \mathbb{R}^{n\times n}$ as

$$\begin{aligned}D_1(e_1,y,u) &:= \frac{\tau_1(e_1,y,u)\phi_1^T(e_1)}{\|\phi_1(e_1)\|^2}\\ D_2(e_1,y,u,\tilde{\xi}) &:= \frac{\Psi^{-1}\tau_2(e_1,y,u,\tilde{\xi})\phi_1^T(e_1)}{\|\phi_1(e_1)\|^2}\end{aligned} \tag{10}$$

Post-multiplying both sides of (10) by $\phi_1(e_1)$ and using the fact that

$$\phi_1^T(e_1)\phi_1(e_1) = \|\phi_1(e_1)\|^2 \tag{11}$$

it follows

$$\begin{aligned} \tau_1(e_1, y, u) &= D_1(e_1, y, u)\phi_1(e_1) \\ \tau_2(e_1, y, u, \tilde{\xi}) &= \Psi D_2(e_1, y, u, \tilde{\xi})\phi_1(e_1) \end{aligned} \tag{12}$$

Remark 2.6. Eqs. (9) and (12) imply that the vector functions $f_1(\cdot)$ and $\tilde{f}_2(\cdot)$ are not necessary to be globally or locally Lipschitz.

According to (12), (8) can be rewritten as

$$\begin{aligned} \dot{e}_1(t) &= -k_1(y,t)E(\cdot)\phi_1(e_1) + D_1(\cdot)\phi_1(e_1) + E(\cdot)e_2(t) \\ \dot{e}_2(t) &= \Psi(-k_1(y,t)E(\cdot)\phi_1(e_1) + E(\cdot)e_2(t) + D(\cdot)\phi_1(e_1)) \\ &\quad - k_2(y,t)\phi_2(e_1) \end{aligned} \tag{13}$$

where $D(\cdot) = D_1(\cdot) + D_2(\cdot)$. As in Gonzalez et al. (2012), it is assumed that the terms $D(\cdot)$ satisfy (almost everywhere)

$$\|D(\cdot)\| \le d(y,t) \tag{14}$$

where $d(y,t)$ represents an upper bound of $D(\cdot)$. Using the fact in (7), (13) is equivalent to

$$\begin{aligned} \dot{e}_1(t) &= -k_1(y,t)E(\cdot)\phi_1(e_1) + D_1(\cdot)\phi_1(e_1) + E(\cdot)e_2(t) \\ \dot{e}_2(t) &= (\nabla_{e_1}\phi_1)\Xi(e_1)(-k_1(y,t)E(\cdot)\phi_1(e_1) + E(\cdot)e_2(t) \\ &\quad + D(\cdot)\phi_1(e_1)) + (\nabla_{e_1}\phi_1)(-k_2(y,t)\phi_1(e_1)) \end{aligned} \tag{15}$$

where $\Xi(e_1) = (\nabla_{e_1}\phi_1)^{-1}\Psi$. By calculating $\nabla_{e_1}\phi_1$ from (6), it follows

$$\nabla_{e_1}\phi_1 = \left(\frac{1}{2\|e_1\|^{\frac{1}{2}}} + k_3\right)I \tag{16}$$

Since by assuming $k_3 > 0$ in (6), $\nabla_{e_1}\phi_1$ is positive definite and thus $\Xi(e_1)$ is well-defined and satisfies

$$\|\Xi(e_1)\| < \frac{\lambda_M}{k_3} \tag{17}$$

Now define

$$M(t) := \begin{bmatrix} M_{11}(t) & M_{12}(t) \\ M_{21}(t) & M_{22}(t) \end{bmatrix} \tag{18}$$

where

$$\begin{aligned} M_{11}(t) &= -k_1(y,t)E(\cdot) + D_1(\cdot) \\ M_{12}(t) &= E(\cdot) \\ M_{21}(t) &= -k_2(y,t) - \Xi(e_1)(k_1(y,t)E(\cdot) - D(\cdot)) \\ M_{22}(t) &= \Xi(e_1)E(\cdot) \end{aligned} \tag{19}$$

Define $\zeta(t) = \begin{bmatrix} \phi_1^T(e_1) & e_2^T(t) \end{bmatrix}^T$, then from (15)

$$\dot{\zeta}(t) = ((\nabla_{e_1}\phi_1) \otimes I_2)M(t)\zeta(t) \tag{20}$$

The main contribution of this paper is shown in the following theorem.

Theorem 2.1. *Assume for some known time varying matrix function $E(y,u,t)$, inequality (14) is satisfied. If the modulation function $k_1(y,t)$ satisfies*

$$\begin{aligned} k_1(y,t) > &\frac{k_3(\delta_1+\delta_2-\beta)^2 d(y,t)^2}{2\beta^2\delta_1\delta_2} + \frac{\delta_2(\delta_1+\delta_2)^2}{2\beta^2\delta_1 k_3} \\ &+ \frac{(\delta_1+\delta_2+\beta)(\delta_1+\delta_2)d(y,t)}{\beta^2\delta_1} \end{aligned} \tag{21}$$

and the modulation function $k_2(y,t)$ is defined as

$$k_2(y,t) = \frac{\beta}{2k_3}k_1(y,t) \tag{22}$$

where $\beta \in (0 \quad \delta_1)$ and $k_3 > 0$ are positive design scalars to be selected. Then, e_1 and e_2 will approach to zero in finite time.

Proof. Define a quadratic Lyapunov function $V(t) = \zeta^T(t)P\zeta(t)$ where the matrix P can be written as

$$P = \begin{bmatrix} p_1 I & -I \\ -I & p_2 I \end{bmatrix} \tag{23}$$

where the scalars p_1 and p_2 are selected as

$$p_1 = (1 + \frac{\beta}{\delta_2})/2k_3 \quad \text{and} \quad p_2 = 2k_3 \tag{24}$$

In this proof, the time and parameter dependence is dropped from the notation. It can be verified from (24) the matrix P is positive definite since p_1 and p_1 are positive scalars and $p_1p_2 > 1$. This particular choice of p_1 and p_2 will be exploited in the sequel.

Define $Q = -(PM + M^TP)$ and the derivative of V is given by

$$\begin{aligned} \dot{V} &= \zeta^T P((\nabla_{e_1}\phi_1) \otimes I_2)M\zeta + \zeta^T M^T((\nabla_{e_1}\phi_1) \otimes I_2)P\zeta \\ &= \zeta^T((\nabla_{e_1}\phi_1) \otimes I_2)PM\zeta + \zeta^T M^T P((\nabla_{e_1}\phi_1) \otimes I_2)\zeta \\ &= -(\nabla_{e_1}\phi_1)\zeta^T Q\zeta \end{aligned} \tag{25}$$

Partition Q as

$$Q = \begin{bmatrix} Q_{11} & * \\ Q_{21} & Q_{22} \end{bmatrix} \tag{26}$$

where

$$\begin{aligned} Q_{11} &= p_1(k_1E - D_1 + k_1E^T - D_1^T) \\ &\quad - (2k_2 + \Xi(k_1E - D) + (k_1E^T - D^T)\Xi^T) \\ &= p_1(k_1(E + E^T) - D_1 - D_1^T) \\ &\quad - (2k_2 + k_1(\Xi E + E^T\Xi^T) - \Xi D - D^T\Xi^T) \end{aligned} \tag{27}$$

$$\begin{aligned} Q_{21} &= -(k_1E - D_1) + p_2(k_2 + \Xi(k_1E - D)) \\ &\quad - p_1E^T + E^T\Xi^T \\ &= -k_1E + D_1 + p_2k_2 + p_2\Xi(k_1E - D) \\ &\quad - p_1E^T + E^T\Xi^T \end{aligned} \tag{28}$$

and

$$Q_{22} = E + E^T - p_2(\Xi E + E^T\Xi^T) \tag{29}$$

From (14) and (17), $\lambda_{\min}(Q_{22})$, $\lambda_{\min}(Q_{11})$ and $\lambda_{\max}(Q_{21})$ satisfy the following inequalities

$$\lambda_{\min}(Q_{22}) > q_{22} = 2\delta_1 - 2p_2\frac{\lambda_M}{k_3}\delta_2 \tag{30}$$

$$\begin{aligned} \lambda_{\min}(Q_{11}) > q_{11} &= 2p_1(\delta_1k_1 - d) - 2(k_2 + \frac{\lambda_M}{k_3}(k_1\delta_2 + d)) \\ &= 2k_1(p_1\delta_1 - \frac{\lambda_M}{k_3}\delta_2) - 2k_2 - 2(p_1 + \frac{\lambda_M}{k_3})d \end{aligned} \tag{31}$$

$$\begin{aligned} \lambda_{\max}(Q_{21}) < q_{21} &= -k_1\delta_1 + d + p_2(k_2 + \frac{\lambda_M}{k_3}(k_1\delta_2 + d)) \\ &\quad + (p_1 + \frac{\lambda_M}{k_3})\delta_2 \end{aligned} \tag{32}$$

From the definitions of q_{21} and q_{22} in (29) and (30), the following equality is established

$$q_{21} = -k_1\frac{q_{22}}{2} + p_2k_2 + (1 + p_2\frac{\lambda_M}{k_3})d + (p_1 + \frac{\lambda_M}{k_3})\delta_2 \tag{33}$$

Since $p_1 = (1 + \frac{\beta}{\delta_2})/p_2$ from (24), q_{11} in (31) can be written as

$$\begin{aligned} q_{11} &= \frac{2}{p_2}k_1\frac{\beta\delta_1}{\delta_2} + \frac{2}{p_2}(k_1(\delta_1 - p_2\frac{\lambda_M}{k_3}\delta_2) - p_2k_2) \\ &\quad - 2(p_1 + \frac{\lambda_M}{k_3})d \\ &= \frac{2}{p_2}k_1\frac{\beta\delta_1}{\delta_2} + \frac{2}{p_2}(k_1\frac{q_{22}}{2} - p_2k_2) - 2(p_1 + \frac{\lambda_M}{k_3})d \end{aligned} \tag{34}$$

Substituting p_2 from (24) and λ_M from (5) into (30) yields

$$q_{22} = 2\beta \tag{35}$$

Then from the definition of k_2 in (22), it follows

$$-k_1\frac{q_{22}}{2} + p_2k_2 = 0 \tag{36}$$

Also from (5) and p_1 in (24), the following equality is established

$$(p_1 + \frac{\lambda_M}{k_3})\delta_2 = \frac{\delta_1 + \delta_2}{k_3} \tag{37}$$

Then substituting (36)–(37) into (33) and (34) yields

$$q_{11} = \frac{2}{p_2}k_1\frac{\beta\delta_1}{\delta_2} - \frac{2(\delta_1 + \delta_2)d}{k_3\delta_2} = \frac{k_1\beta\delta_1 - 2(\delta_1 + \delta_2)d}{k_3\delta_2} \tag{38}$$

$$q_{21} = (1 + p_2\frac{\lambda_M}{k_3})d + \frac{\delta_1 + \delta_2}{k_3} = \frac{\delta_1 + \delta_2 - \beta}{\delta_2}d + \frac{\delta_1 + \delta_2}{k_3} \tag{39}$$

From the definition of k_1 in (21) and the choice of p_1 and p_2 in (24), it can be verified from (38) and (39) that $q_{11}q_{22} - q_{21}^2 > 0$. Since $q_{21} > \|Q_{21}\|$ and $q_{22} < \lambda_{\min}(Q_{22})$, it follows $q_{22} > 1/\|Q_{22}^{-1}\|$ and $q_{11} - \|Q_{21}^T\|\|Q_{22}^{-1}\|\|Q_{21}\| > 0$. Using $\lambda_{\min}(Q_{11}) > q_{11}$, $Q_{11} - Q_{21}^TQ_{22}^{-1}Q_{21} > 0$ and the matrix Q in (26) is positive definite.

From (16) and (25)

$$\dot{V} \le -\lambda_{\min}(Q)(\frac{1}{2\|\sigma\|^{\frac{1}{2}}} + k_3)\|\zeta\|^2 \tag{40}$$

and using the fact that $\frac{V}{\lambda_{\max}(P)} \le \|\zeta\|^2 \le \frac{V}{\lambda_{\min}(P)}$

$$\dot{V} \le -\lambda_{\min}(Q)\frac{1}{2\|\sigma\|^{\frac{1}{2}}}\frac{V}{\lambda_{\max}(P)} - k_3\frac{\lambda_{\min}(Q)}{\lambda_{\max}(P)}V \tag{41}$$

Also since $\zeta = \begin{bmatrix}\phi_1^T(\sigma) & z^T\end{bmatrix}^T$,

$$(\frac{1}{\|\sigma\|^{\frac{1}{2}}} + k_3)\|\sigma\| = \|\phi_1\| \le \|\zeta\| \le \frac{\sqrt{V}}{\sqrt{\lambda_{\min}(P)}} \tag{42}$$

and therefore

$$\|\sigma\|^{\frac{1}{2}}(1 + k_3\|\sigma\|^{\frac{1}{2}}) \le \frac{\sqrt{V}}{\sqrt{\lambda_{\min}(P)}} \tag{43}$$

From (43) it follows $\|\sigma\|^{\frac{1}{2}} \le \frac{\sqrt{V}}{\sqrt{\lambda_{\min}(P)}}$. Consequently, by substituting $\|\sigma\|^{-\frac{1}{2}} \ge \frac{\sqrt{\lambda_{\min}(P)}}{\sqrt{V}}$ into (41) yields

$$\dot{V} \le -\frac{\lambda_{\min}(Q)\sqrt{\lambda_{\min}(P)}}{2\lambda_{\max}(P)}\sqrt{V} - \frac{k_3\lambda_{\min}(Q)}{\lambda_{\max}(P)}V \tag{44}$$

As argued in Gonzalez et al. (2012), from Lyapunov's Theorem for Differential Inclusions (Deimling, 1992), $e_1 \to 0$ and $e_2 \to 0$ in finite time for any initial conditions. ■

During sliding, $e_1 \to 0$ and therefore $\hat{x}_1 \to x_1$. Also since $e_2 \to 0$, $\hat{x}_2 - \tilde{x}_2 + \Psi e_1 \to 0$ and then $\hat{x}_2 \to \tilde{x}_2$. Let $\hat{x}_2 = \text{col}(\hat{x}_{21}, \hat{x}_{22})$, then $\hat{x}_{21} \to x_2$.

In the next section, the above theoretical developments will be applied to an icing accretion estimation problem.

3. Icing accretion estimation

3.1. Problem formulation

Since icing accretion increases the drag acting on the aircraft, the design scheme in Section 2 will be employed to monitor the change of the drag coefficient. Notice that the change of drag may be caused by various reasons, e.g. engine failures, damage of aerodynamic structures, problems with a landing gear retraction and other severe weather conditions. Here it is assumed that the change of the drag coefficient is mainly caused by icing accretion. In the face of icing accretion, the change of the drag coefficient is given by

$$\delta C_D = C_{D,act} - C_{D,exp} \tag{45}$$

where $C_{D,act}$ is the actual drag coefficient and $C_{D,exp}$ represents the expected drag coefficient given by

$$C_{D,exp} = C_{D0} + kC_L^2 \tag{46}$$

where C_{D0} is the known zero-lift coefficient, C_L represents the lift coefficient and k is the lift-independent drag coefficient factor obtained experimentally from the earlier flight tests and for the Jetstream J31 (Lawson et al., 2017).

During a steady level flight, the aircraft lift $L = mg$ and thus C_L is calculated as

$$C_L = \frac{L}{0.5\rho_0SV_T^2} = \frac{mg}{0.5\rho_0SV_T^2} \tag{47}$$

where the parameter ρ_0 is the air density of International Standard Atmosphere (ISA) at sea level, S denotes the wing area and V_T represents true airspeed.

The crucial longitudinal nonlinear dynamic equation of the fixed wing aircraft during a steady level flight is

$$\begin{aligned} \dot{V}_T &= \frac{F_x\cos\alpha + F_z\sin\alpha}{m} \\ \dot{\alpha} &= \frac{-F_x\sin\alpha + F_z\cos\alpha}{mV_T} + q \end{aligned} \tag{48}$$

where the body-axis aerodynamic forces are given by

$$\begin{aligned} F_x &= -\bar{q}S(C_D\cos\alpha - C_L\sin\alpha) + T_{tol} - mg\sin\theta \\ F_z &= -\bar{q}S(C_D\sin\alpha + C_L\cos\alpha) + mg\cos\theta \end{aligned} \tag{49}$$

Substituting (49) into (48) yields

$$\begin{aligned} \dot{V}_T &= -\frac{\rho_0V_T^2S}{2m}(C_{D,exp} + \delta C_D) + \frac{T_{tol}}{m}\cos\alpha + g\sin(\alpha - \theta) \\ \dot{\alpha} &= -\frac{T_{tol}}{mV_T}\sin\alpha + \frac{g}{V_T}(\sin\theta\sin\alpha + \cos\theta\cos\alpha - 1) + q \end{aligned} \tag{50}$$

Let $x_1 = [V_T \quad \alpha]^T$, $x_2 = [-\delta C_D \quad q]^T$ and $y = V_T$, (50) is equivalent to

$$\dot{x}_1 = f(x_1, t) + E(y, t)x_2 \tag{51}$$

where $E(y, t) = \text{diag}(\frac{\rho_0y^2S}{2m}, 1)$ is positive definite and

$$f(x_1, t) = \begin{bmatrix} -\frac{\rho_0V_T^2S}{2m}C_{D,exp} + \frac{T_{tol}}{m}\cos\alpha + g\sin(\alpha - \theta) \\ -\frac{T_{tol}}{mV_T}\sin\alpha + \frac{g}{V_T}(\sin\theta\sin\alpha + \cos\theta\cos\alpha - 1) \end{bmatrix} \tag{52}$$

Since the observability maps

$$\begin{bmatrix} y \\ \dot{y} \end{bmatrix} = \begin{bmatrix} x_1 \\ f(x_1, t) + E(y, t)x_2 \end{bmatrix} \tag{53}$$

is globally invertible (Khalil, 2002) and thus the uniformly observability imposed in Assumption 2.1 is verified. Define $e_1 = \hat{x}_1 - x_1$,

Fig. 1. Jetstream J31 aircraft.

(a) icing on the wing (b) icing on the tube

Fig. 2. Natural icing accretion during flight test.

the observer is created as

$$\begin{aligned}\dot{\hat{x}}_1 &= -k_1(y,t)E(y,t)\phi_1(e_1) + E(y,t)(\hat{x}_2 + \Psi e_1) \\ &\quad + f(\hat{x}_1, t) \\ \dot{\hat{x}}_2 &= -k_2(y,t)\phi_2(e_1)\end{aligned} \tag{54}$$

3.2. Flight data collection

To further assess the effectiveness and applicability of the design scheme in this paper, flight test data obtained from the Cranfield University's Jetstream J31 aircraft (Fig. 1) is used in an offline evaluation.[1] This aircraft is a manned fixed wing aircraft cleared to operate in icing conditions conform to either FAR/CS23 or FAR/CS25 certification standards (see Fig. 1).

During the flight test, the aircraft flies in a steady straight level and information about the actual mass, thrust, the aircraft altitude, the actual center of the gravity information, and indicated airspeed are available onboard. Also it is noticed that engine failures, damage of aerodynamic structures and problems with a landing gear retraction do not exist and the weather conditions are not severe during the flight tests. Thus the drag increase is assumed to be due to the change of the zero-lift coefficient caused by icing accretion.

During the flight test, only the longitudinal motion was considered. The velocity was maintained via auto-throttle despite icing accretion. Only the elevator angle or rather AoA remains close to a free trim variable which is increased in icing conditions since the wing lift curve slope decreases and less lift is produced at the same AoA.

3.3. Performance validation using flight test data

The zero-lift coefficient C_{D0} and the lift-independent drag coefficient factor k, obtained from the flight tests for the Jetstream J31, are selected as $C_{D0} = 0.0375$ and $k = 0.0588$, respectively. The air density ρ_0 is chosen as 1.225 kg/m^2, the wing area is $S = 25.2$ m^2 and the aircraft mass is $m = 5946$ kg.

[1] In this aircraft, the avionics system is not equipped for onboard validation.

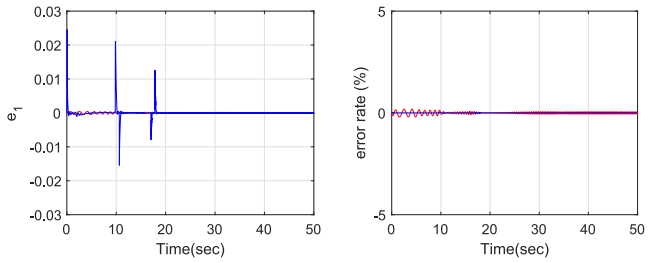

(a) The state estimation error e_1 and estimation error rates comparing with states

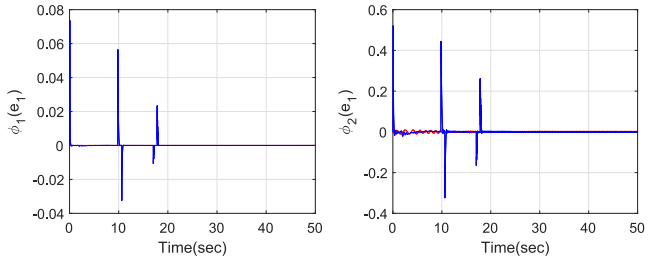

(b) The functions $\phi_1(e_1)$ and $\phi_2(e_1)$

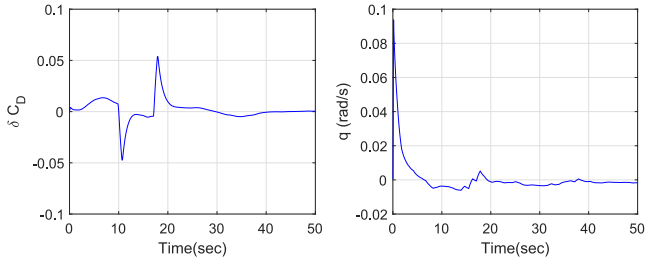

(c) The change of C_D and the q estimation error

Fig. 3. Icing free at 7000 ft.

During the flight test, the Jetstream was flown at given trimmed steady flight conditions, at a velocity (indicated airspeed) of 120 kts, first in the absence of icing, to obtain baseline values at an altitude of 7000 ft. Then the aircraft descended to 4500 ft and flew into cloud in conditions favourable for natural ice accretion. To validate the observer performance, the aircraft was also trimmed at the same airspeed of 120 kts at 4500 ft. To allow for performance degradation to be evaluated more effectively, the de-icing system on the wings and tailplane was not activated; however, anti-icing protection on the propellers and engine inlets was always activated to comply with the aircraft flight manual. This does not have an effect on the results. Values for the ice-affected aircraft began to be recorded once a visible layer was observed on the leading edges of the lifting surfaces (see Fig. 2). After completion of the successive testing phase, the de-icing boots were activated, and the aircraft returned to a clean condition.

The tuning process contains the following steps: (i) using the fact $E(y,t) = \text{diag}(\frac{\rho_0 y^2 S}{2m}, 1)$ and computing δ_1 and δ_2 from the recorded true airspeed and the aircraft mass measurements to satisfy Assumption 2.2; (ii) choosing $\beta \in (0 \;\; \delta_1)$ and determining the design matrix Ψ from (5); (iii) solving the function $d(\cdot)$ from the upper bounds of $D(\cdot)$ defined in (14); (iv) selecting the positive scalar k_3; (v) according to (21) and (22), computing k_1 and k_2 online from $\delta_1, \delta_2, \beta, k_3$ and $d(\cdot)$. During the simulation, the values of the design scalars are selected as $\beta = 0.5$ and $k_3 = 5$.

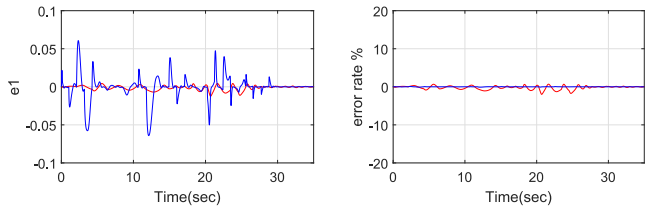

(a) The state estimation error e_1 and estimation error rates comparing with states

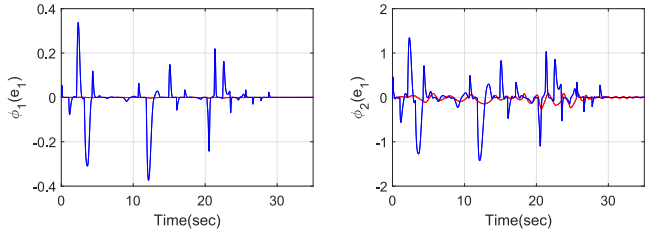

(b) The functions $\phi_1(e_1)$ and $\phi_2(e_1)$

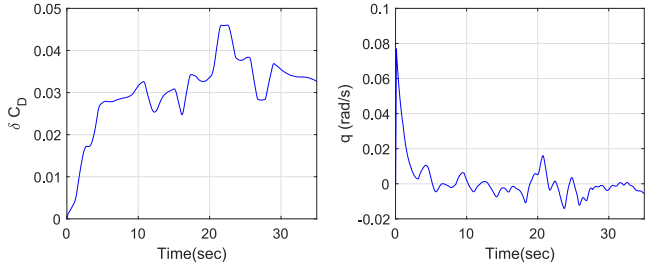

(c) The change of C_D and the q estimation error

Fig. 4. Natural icing condition at 4500 ft.

The matrix Ψ is in the form of $\Psi = \text{diag}(0.0463, 0.3704)$. The scalars $\delta_1 = 11.2559$ and $\delta_2 = 11.6143$ are calculated from the recorded V_T and m, which verifies Assumption 2.2.

The icing estimation results at an altitude of 7000 ft (no icing) and 4500 ft (icing condition) are shown in Figs. 3–4. The flight data associated with the altitudes of 7000 ft and 4500 ft are recorded for 50 s and 35 s, respectively. As shown in Figs. 3(a) and 4(a), the state estimation errors e_1 approach to zero despite the various flight conditions and the natural icing accretion. It can also be seen from Figs. 3(a) and 4(a) that the estimation error rates compared with the actual states are low for both icing free and icing accretion cases. The discontinuous terms $\phi_1(e_1)$ and $\phi_2(e_1)$ defined in (6) are shown in Fig. 3(b) (no icing) and Fig. 4(b) (natural icing condition). Notice that the spikes in Figs. 3(b) and 4(b) are caused by the small thrust variations created by the pilot. The changes of the drag coefficient δC_D without and with icing accretion are shown in Figs. 3(c) and 4(c), respectively. It can be seen from Fig. 3(c) that, at an altitude of 7000 ft, the change of the drag coefficient estimate δC_D in the early part of the experiment is close to zero in the ice-free condition. Furthermore, Fig. 4(c) describes the change of the drag coefficient due to icing accretion at an altitude of 4500 ft. It can be seen from Fig. 4(c) that the amplitude of the drag coefficient was increased from 0 to $0.03 \sim 0.04$ due to the build up of ice. This implies an increased airframe drag needs to be sensed by the pilot. Since the pitch rate measurements are not available during the flight test, the actual pitch rate, used to verify the accuracy of the pitch rate estimation, is computed via applying the pitch angle measurements to a robust differentiator (Levant, 1998). The pitch rate estimation errors are shown in Figs. 3(c) and 4(c), respectively. Clearly, the scheme proposed in this paper allows the pitch rate estimation errors to converge towards near zero in the presence of icing accretion.

4. Conclusion

In this paper, the problem of icing diagnosis was addressed using a multivariable super twisting observer. Through appropriately using the state dependent gains, the proposed observer scheme can estimate the unknown variable scaled by the known state dependent matrix function. Real flight data under natural icing conditions, collected from a flight test were used to illustrate the effectiveness of the approach. Accurate results demonstrate that the icing severity and the unreliable sensor measurement are able to be estimated in finite time simultaneously. Future works mainly focus on a comparative study of various icing diagnosis methods and the development of an integrated icing fault tolerant control scheme in the face of large pitch excitations despite the reduced stall AoA.

References

Alwi, H., Edwards, C., & Tan, C. P. (2011). *Fault detection and fault-tolerant control using sliding modes*. Springer.

Armanini, S. F., Polak, M., Gautrey, J. E., Lucas, A., & Whidborne, J. F. (2016). Decision-making for unmanned aerial vehicle operation in icing conditions. *CEAS Aeronautics Journal*, *7*, 663–675.

BBC (2017). Myanmar plane: Bad weather blamed for Andaman Sea crash. https://www.bbc.co.uk/news/world-asia-40653524.

Blanke, M., Kinnaert, M., Lunze, J., & Staroswiecki, M. (2016). *Introduction to diagnosis and fault-tolerant control*. Heidelberg: Springer Berlin Heidelberg.

Caliskan, F., Aykan, R., & Hajiyev, C. (2008). Aircraft icing detection, identification, and reconfigurable control based on Kalman filtering and neural networks. *Journal of Aerospace Engineering*, *21*, 51–60.

Castillo, I., Fridman, L., & Moreno, J. A. (2018). Super-twisting algorithm in presence of time and state dependent perturbations. *International Journal of Control*, *91*, 2535–2548.

Chen, L., Alwi, H., Edwards, C., & Sato, M. (2020). Flight evaluation of a sliding mode online control allocation scheme for fault tolerant control. *Automatica*, *114*, Article 108829.

Chen, L., Alwi, H., Edwards, C., & Sato, M. (2022). Flight evaluation of an LPV sliding mode observer for sensor ftc. *IEEE Transactions on Control Systems Technology*, *30*, 1319–1327.

Chen, L., Edwards, C., & Alwi, H. (2019). Sensor fault estimation using LPV sliding mode observers with erroneous scheduling parameters. *Automatica*, *101*, 66–77.

Chen, J., & Patton, R. J. (1999). *Robust model-based fault diagnosis for dynamic systems*. Kluwer academic publishers.

Cristofaro, A., & Johansen, T. A. (2015). An unknown input observer approach to icing detection for unmanned aerial vehicles with linearized longitudinal motion. In *American control conference* (pp. 207–213).

Cristofaro, A., Johansen, T. A., & Aguiar, A. P. (2015). Icing detection and identification for unmanned aerial vehicles: Multiple model adaptive estimation. In *European control conference* (pp. 1651–1656).

Deimling, K. (1992). *Multivalued differential equations*. Berlin, Germany: Walter de Gruyer.

Ding, S. X. (2013). *Model-based fault diagnosis techniques*. London: Springer.

Dong, Y. (2018). An application of deep neural networks to the in-flight parameter identification for detection and characterization of aircraft icing. *Aerospace Science and Technology*, *77*, 34–49.

Edwards, C., Lombaerts, T., & Smaili, H. (2010). *Fault tolerant flight control: a benchmark challenge*. Springer.

Edwards, C., & Spurgeon, S. K. (1998). *Sliding mode control: theory and applications*. London, U.K: Taylor & Francis.

Efimov, D., Edwards, C., & Zolghadri, A. (2016). Enhancement of adaptive observer robustness applying sliding mode techniques. *Automatica*, *72*, 53–56.

Elleuch, I., Khedher, A., & Othman, K. B. (2018). Design of a proportional integral observer based on sliding mode principle for uncertain Takagi–Sugeno fuzzy systems: Applications to a Turbo-reactor. *International Journal of Automation and Control*, *12*, 179–194.

FAA, . (2020). In-flight icing. https://www.faa.gov/nextgen/programs/weather/awrp/ifi/.

Filippov, A. F. (1988). *Differential equations with discontinuous right-hand side*. Dordrecht, the Netherlands: Kluwer.
Gauthier, J. P., Hammouri, H., & Othman, S. (1992). A simple observer for nonlinear systems applications to bioreactors. *IEEE Transactions on Automatic Control*, *37*, 875–880.
Gonzalez, T., Moreno, J. A., & Fridman, L. (2012). Variable gain super-twisting sliding mode control. *IEEE Transactions on Automatic Control*, *57*, 2100–2105.
Goupil, P., Dayre, R., & Brot, P. (2014). From theory to flight tests: Airbus flight control system TRL5 achievements. In *IFAC world congress*.
Guzman, E., & Moreno, J. A. (2015). Super-twisting observer for second-order systems with time-varying coefficient. *IET Control Theory & Applications*, *9*, 553–562.
Khalil, H. (2002). *Nonlinear systems* (3rd ed.). Prentice Hall.
Lampton, A., & Valasek, J. (2007). Prediction of icing effects on the dynamic response of light airplanes. *Journal of Guidance, Control, and Dynamics*, *30*, 722–732.
Lawson, N. J., Jacques, H., Gautrey, J. E., Cooke, A. K., Holt, J. C., & Garry, K. P. (2017). Jetstream 31 national flying laboratory: Lift and drag measurement and modelling. *Aerospace Science and Technology*, *60*, 84–95.
Levant, A. (1998). Robust exact differentiation via sliding mode technique. *Automatica*, *34*, 379–384.
de Loza, A. F., Bejarano, F. J., & Fridman, L. (2013). Unmatched uncertainties compensation based on high-order sliding mode observation. *Internationl Journal of Robust and Nonlinear Control*, *23*, 754–764.
Marcos, A., Waitman, S., & Sato, M. (2021). Fault tolerant LPV flight control design, verification and validation. *Journal of the Franklin Institute*, *359*, 653–676.
Melody, J. W., Başar, T., Perkins, W. R., & Voulgaris, P. G. (2000). Parameter identification for inflight detection and characterization of aircraft icing. *Control Engineering Practice*, *8*, 985–1001.
Melody, J. W., Hillbrand, T., Başar, T., & Perkins, W. R. (2001). $\mathcal{H}_\infty$ Parameter identification for inflight detection of aircraft icing: the time-varying case. *Control Engineering Practice*, *9*, 1327–1335.
Miller, R., & Ribbens, W. (1999). Detection of the loss of elevator effectiveness due to aircraft icing. In *37th Aerospace Sciences Meeting and Exhibit*. AIAA.
Moreno, J. A., & Alvarez, J. (2014). A weighted variable gain super-twisting observer for the estimation of kinetic rates in biological systems. *Journal of Process Control*, *24*, 957–965.
Moreno, J. A., Rios, H., Ovalle, L., & Fridman, L. (2022). Multivariable super-twisting algorithm for systems with uncertain input matrix and perturbations. *IEEE Transactions on Automatic Control*, 6716–6722.
Nagesh, I., & Edwards, C. (2014). A multivariable super-twisting sliding mode approach. *Automatica*, *50*, 984–988.
N'Faly, C. (2016). *Accident on 24 July 2014 in the region of gossi in mali to the md-83 registered ec-ltv operated by swiftair s.a.*. Commission d'enquete sur les accidents et incidents d'aviation civile.
Oliveira, T. R., Estrada, A., & Fridman, L. (2017). Global and exact HOSM differentiator with dynamic gains for output-feedback sliding mode control. *Automatica*, *81*, 156–163.
Oliveira, T. R., Rodrigues, V. H. P., Estrada, A., & Fridman, L. (2018). Output-feedback variable gain super-twisting algorithm for arbitrary relative degree systems. *International Journal of Control*, *9*, 2043–2059.
Rodrigues, V. H. P., & Oliveira, T. R. (2018). Global adaptive HOSM differentiators via monitoring functions and hybrid state-norm observers for output feedback. *International Journal of Control*, *91*, 2060–2072.
Rodrigues, V. H. P., & Oliveira, T. R. (2022). Multivariable variable-gain super-twisting control via output feedback for systems with arbitrary relative degrees. *International Journal of the Adaptive Control Signal Processing*, *36*, 230–250.
Rotondo, D., Cristofaro, A., Johansen, T. A., Nejjari, F., & Puig, V. (2018). Diagnosis of icing and actuator faults in UAVs using LPV unknown input observers. *Journal of Intelligent and Robotic Systems*, *91*, 651–665.
Rotondo, D., Cristofaro, A., Johansen, T. A., Nejjari, F., & Puig, V. (2019). Robust fault and icing diagnosis in unmanned aerial vehicles using LPV interval observers. *International Journal of Robust and Nonlinear Control*, *29*, 5456–5480.
Sastry, S., & Bodson, M. (1989). *Adaptive control: stability, convergence and robustness*. London: Prentice-Hall.
Schuchard, E. A., Melody, J. W., Başar, T., Perkins, W. R., & Voulgaris, P. (2000). Detection and classification of aircraft icing using neural networks. In *38th Aerospace Sciences Meeting and Exhibit*. AIAA.
Sorensen, K. L., Blanke, M., & Johansen, T. A. (2015). Diagnosis of wing icing through lift and drag coefficient change detection for small unmanned aircraft. *IFAC-PapersOnLine*, *48*, 541–546.
Transportation Safety Board of Canada (2021). Loss of control and collision with terrain.
Utkin, V. (1992). *Sliding modes in control and optimization*. Springer.
Vidal, P. V. N. M., Nunes, E. V. L., & Hsu, L. (2017). Output-feedback multivariable global variable gain super-twisting algorithm. *IEEE Transactions on Automatic Control*, 2999–3005.
Yan, X., & Edwards, C. (2008). Adaptive sliding-mode-observer-based fault reconstruction for nonlinear systems with parametric uncertainties. *IEEE Transactions on Industrial Electronics*, *55*, 4029–4036.
Zhang, Y., & Jiang, J. (2008). Bibliographical review on reconfigurable fault-tolerant control systems. *Annual Reviews in Control*, *32*, 229–252.

Lejun Chen obtained his Ph.D. degree from the intelligent system group, the University of York. He has been appointed as a Lecturer in the Department of Electronic and Electrical Engineering at University College London since 2022. He is also the Visiting Fellow at Cranfield University. His research interests are in navigation and control, and their applications to aerospace, robotic and autonomous systems.

James F. Whidborne is Professor of Control Engineering in the Centre for Aeronautics at Cranfield University. He received his BA in engineering from the Cambridge University, and M.Sc. and Ph.D. in systems and control from the University of Manchester Institute of Science and Technology (UMIST). Following positions at the University of Leicester and Kings College London, he joined Cranfield University in 2004. He is a Chartered Engineer, a Member of the IET and a Senior Member of the IEEE. He is Vice-Chair of the IFAC Technical Committee on Control Design, is a Member IFAC Industry Committee, and is on the IMech E Mechatronics, Informatics and Control Group Committee. He has over 200 refereed research publications, including three books. His research interests are in the theory and application of advanced control, particularly in the area of aeronautics.